

# Water activity regulates CO<sub>2</sub> reduction in gas-diffusion electrodes

Nathan T. Nesbitt<sup>\*a</sup> and Wilson A. Smith<sup>\*a,b</sup>

Submitted 15th January 2021  
doi: 10.26434/chemrxiv.13571141

Electrolysis of CO<sub>2</sub> at gas-diffusion electrodes (GDEs) has typically been limited by the supply of gas to the electrocatalyst, overshadowing the importance of the supply of water. However, at high current densities that approach 1 A cm<sup>-2</sup>, where the electrolyte becomes highly concentrated in the catalyst layer of a GDE, the activity of water and solutes deviate from their bulk dilute-solution values, potentially slowing reaction rates and changing reaction equilibrium potentials. In addition, as flow plates for the gas stream are introduced to enable larger electrodes and high single pass conversion of CO<sub>2</sub> to product, variations in the gas composition will become important. By drawing upon literature for the oxygen reduction reaction (ORR), here we explain how to account for these effects in future modelling and experimental work, with particular attention to accurate use of the Nernst equation for electrode potentials and the Arrhenius equation for reaction rates. Specifically, using measurements of KOH solvent and solute activity reported in literature, and assuming the second protonation of CO<sub>2</sub> by water as the rate-determining step, we show the Nernst equation dilute-solution approximation of the CO<sub>2</sub> to CO equilibrium potential to be accurate below 5 M KOH, but has a 74 mV error when increasing the concentration up to 10 M KOH. Finally, a simple one-dimensional model of a serpentine flow-field on a GDE demonstrated that a reactor with constant pressure of 1 bar and 1 A cm<sup>-2</sup> at the inlet had only ~0.3 A cm<sup>-2</sup> at the outlet for a conversion in CO<sub>2</sub> partial pressure from 0.90 to 0.48 bar, showing the significant practical implications of this work.

## Introduction

### Background

Electrochemical CO<sub>2</sub> reduction (CO<sub>2</sub>R) is a rapidly developing technology that, if successfully commercialized, may provide a means to produce fuels and commodity chemical feedstocks with renewable energy, rather than from fossil fuels. CO<sub>2</sub>R was originally performed in so-called aqueous H-cells, which had the cathode fully immersed in a liquid electrolyte and CO<sub>2</sub> supplied to the cathode by dissolution into the electrolyte. Subsequently, current densities over 10x higher were achieved by using reactors with gas-diffusion electrode (GDE) cathodes.<sup>1</sup> GDEs position the interface of gas-phase CO<sub>2</sub> and liquid electrolyte in close proximity to the catalyst layer (CL), providing fast diffusion of CO<sub>2</sub> in the gas-phase, as well as fast diffusion across mere 10s to 1000s of nanometers of liquid between the gas-phase and the electrocatalyst. The CO<sub>2</sub> electrolysis field has grown considerably in the past years, and by using the GDE architecture has been able to increase operational current densities above 1 A cm<sup>-2</sup>.<sup>2–5</sup>

The high performance of GDE devices has emphasized the importance of a plentiful supply of CO<sub>2</sub> via a facile diffusion

pathway. This has encouraged a CO<sub>2</sub>-centric perspective on assessing and improving CO<sub>2</sub>R GDE performance. Here, we give an in-depth explanation of the role of water in a CO<sub>2</sub>R GDE, in particular how water and solute activities likely regulate CO<sub>2</sub>R activity and equilibrium potentials in the CL, and what further computational and experimental work is needed to understand and further optimize the activity of this important chemical reaction.

### Current Status

The transition of the CO<sub>2</sub>R research field to GDE-based architectures has been growing significantly over the past several years. Modelling has kept pace by simulating different water, ionomer, and catalyst distributions in the CL of the GDEs,<sup>6–13</sup> and predicting the corresponding CO<sub>2</sub> and current distributions. Further work has assessed the effect of water flooding in the GDE, a common mode for GDE deactivation during long duration stability tests.<sup>14</sup> These advances have moved the field towards more stable GDEs, with control over water distribution in the GDE to ensure robust pathways for CO<sub>2</sub> to diffuse and react with protons and electrons at catalytic active sites.

Importantly, modelling<sup>6</sup> and experiments<sup>15</sup> have shown that high current densities produce large quantities of OH<sup>-</sup>, which attracts cations and causes elevated concentration and pH of electrolyte in the CL. This elevated electrolyte concentration and pH cause faster conversion of CO<sub>2</sub> into (bi)carbonate, diminishing the CO<sub>2</sub> supply to the CL and increasing electrolyte viscosity, slowing CO<sub>2</sub> diffusion to the CL. The elevated

<sup>a</sup> Materials, Chemical, and Computational Science (MCCS) Directorate, National Renewable Energy Laboratory, Golden, CO 80401, United States of America.

<sup>b</sup> Department of Chemical and Biological Engineering and Renewable and Sustainable Energy Institute (RASEI), University of Colorado Boulder, Colorado 80303, United States.

NN: [nathan.nesbitt@nrel.gov](mailto:nathan.nesbitt@nrel.gov)

WS: [wilson.smith@nrel.gov](mailto:wilson.smith@nrel.gov)

concentrations increase ion density and thereby electrolyte conductivity until they reach 5 molar (M) for NaOH and 7 M for KOH, above which high viscosity lowers the conductivity.<sup>16</sup> Concentrated (5-7 M) KOH electrolytes have also been used intentionally to suppress HER and optimize electrolyte conductivity;<sup>4</sup> however, this comes at the cost of low energy efficiency due to CO<sub>2</sub> conversion to (bi)carbonate<sup>17,18</sup> and, as discussed below, may introduce undesirable changes to water and solute activities.

In one example of the importance of water supply to the CL, by increasing the stirring of the bulk electrolyte, the CL electrolyte concentration was lowered, allowing higher CO<sub>2</sub> concentrations in the CL.<sup>6</sup> In membrane electrode assemblies (MEAs) it was also demonstrated that the water supply, rather than CO<sub>2</sub> supply, limited the device current density.<sup>7</sup>

Another important parameter to incorporate into models and experiments is the water and solute activity at the catalyst surface. The high local electrolyte concentrations in the microenvironment of the CL lowers water activity and increases solute activity, slowing the CO<sub>2</sub>R reaction rate and changing reaction equilibrium potentials. These effects have been commented on in recent modelling literature,<sup>12</sup> but have yet to be directly accounted for in experimental design or modelling work. In recent studies on PtO reduction and the oxygen reduction reaction (ORR), however, the phenomena have been explicitly shown.<sup>19–21</sup> In the following sections, we explore these effects in detail.

## Accounting for Activity Variations in CO<sub>2</sub>R

The following sub-sections discuss the existing experimental and modeling work that demonstrate how water and solute activity affect electrochemical reactions, at what electrolyte concentrations and electrode conditions the effect is non-negligible, and what further work is needed to better understand CO<sub>2</sub>R in GDE and MEA architectures.

### Water and solute activities' effect on reaction equilibrium potential

Here, we give a detailed overview of how water and solute activity are defined and measured, and their influence on the equilibrium potential of electrochemical reactions.

The activity of water represents the availability of water molecules for chemical/physical interactions, such as to hydrate ions in solution, evaporate into the headspace of a vessel, or participate in electrochemical reactions. The water activity ranges from 0 to 1, equal to unity when the water is pure. At low solute concentrations, the activity of water ( $a_{\text{H}_2\text{O}}$ ) can be approximated by the partial pressure of water vapor above the solution ( $p_q$ ) divided by the partial pressure of water vapor above pure water ( $p_0$ ),  $a_{\text{H}_2\text{O}} = p_q/p_0$ . At higher concentrations, a more complicated expression is necessary,<sup>22–24</sup> but it is still derived from the thermodynamic definition of

activity,  $a_q = e^{\mu_q - \mu_q^\theta / RT}$ , where  $\mu_q$  is the chemical potential of the species  $q$  in the condition of interest,  $\mu_q^\theta$  is the chemical potential of the species  $q$  in a defined standard state,  $R$  is the gas constant, and  $T$  is the absolute temperature.

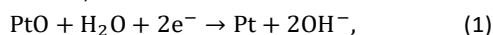
For water activity, the commonly used standard state is pure water. Figure 1a shows the measured water activity as a function of solute concentration for aqueous solutions of KOH and NaOH, common electrolytes for CO<sub>2</sub>R and the oxygen reduction reaction (ORR), respectively. At high solute concentrations, the water activity can drop significantly to below 0.5 for KOH concentrations above 8 M and NaOH concentration above 9 M. While water activity is typically reported against molality (moles of solute per kilogram of solvent) to avoid a temperature dependence, here it has been converted to molarity<sup>25</sup> (moles of solute per liter of solution) for the convenience of the CO<sub>2</sub>R research field, which typically uses molarities; we use the variable  $c$  and unit M to indicate concentrations in molarity.

Solute activity uses a different common choice of standard state to define activity. For dissolved solids and liquids the standard state is a concentration of 1 M, and the activity coefficient goes to one at infinite dilution. Consequently, the activity for a solid or liquid solute is commonly defined with an activity coefficient ( $\gamma_q$ ) and the ratio between a concentration of interest ( $c_q$ ) and the standard 1 M concentration ( $c_q^0$ ), giving  $a_q = \gamma_q(c_q/c_q^0)$  for a given solute  $q$ . Figure 1b shows the activity coefficient for the respective solutes Na<sup>+</sup>, K<sup>+</sup>, and OH<sup>−</sup> of various aqueous solutions of NaOH and KOH. For dissolved gases, a similar convention is used, but with concentration defined by the associated partial pressure ( $p_q$ ) and the standard state at 1 bar partial pressure ( $p_q^0$ ), giving activity as  $a_q = \gamma_q(p_q/p_q^0)$ ; Appendix A shows the derivation of the activity coefficient for dissolved gas (see supplemental information for appendices A–H). Unlike the simple monotonic decrease in water activity with increasing solute concentration, the solute activity is non-monotonic. The ratio  $c_q/c_q^0$  or  $p_q/p_q^0$  just equals the solute molarity or partial pressure given the standard states defined above, but the activity coefficient is more complicated. As shown in Figures F-5 through F-10, the activity coefficient equals 1 at very dilute concentrations, drops below 1 as it approaches 1 M, then increases, reaching 4.2 by 10 M NaOH and reaching 10.4 by 10 M KOH.

In addition to temperature independence, there is another reason that molality is convenient to use when considering high solute concentrations. By its definition, the molality of a solvent cannot change with thermodynamic or process parameters. While much research in electrochemistry uses sufficiently dilute solutions to assume the molarity of water does not change with varying solute concentration, we will see this is not the case for the high electrolyte concentrations in GDE CLs operating at high current densities. As shown in Figure 1c and Figures F-1 through F-4, the molarity of water drops ~10% to 50 M by 7 M KOH or 12 M NaOH.

To improve ease-of-use of water and solute activities for the researchers in the CO<sub>2</sub>R field, we have provided polynomial fit coefficients for water and solute activity vs. molarity in Table C-1. These fits are plotted as solid and dashed lines, respectively, in Figure 1a-b. Plots of the fits against a wider range of molarity and against molality are provided in Figures F-1 through F-17.

To give a clearer demonstration of the effect of water activity on electrochemical reactions, before discussing the more complicated CO<sub>2</sub>R, we first discuss the solid reactant/product pair Pt/PtO at a scanning electrochemical microscope (SECM) probe in different NaOH concentrations. The expected reaction is,



which, assuming unit activity for solids and applying the Nernst equation, has the potential dependence on water and OH<sup>-</sup> activity,<sup>19</sup>

$$E_{\text{PtO/Pt}} = E^0 + \frac{RT}{nF} \ln \frac{a_{\text{H}_2\text{O}}}{a_{\text{OH}^-}^2}. \quad (2)$$

where  $n$  is the number of electrons per PtO molecule,  $R$  the gas constant, and  $T$  absolute temperature.

Figure 1d shows the measured peak potential of PtO reduction,  $E_{\text{PtO red.}}$ , from cyclic voltammograms recorded in various NaOH concentrations. This is used as an approximation for  $E_{\text{PtO/Pt}}$ . Being defined by a standard state of 1 M OH<sup>-</sup>, the OH<sup>-</sup> activity should increase along with NaOH concentration. Water activity, on the other hand, defined by the standard state of pure water, will decrease with increasing NaOH concentration. The ratio of these activities determines  $E_{\text{PtO red.}}$ , and the semi-log plot in Figure 1d thus shows the rate of change of this ratio with increasing NaOH molarity. A change in slope at ~10 M NaOH suggests this is a critical concentration for this electrochemical reaction, above which  $E_{\text{PtO red.}}$  is much more sensitive to the NaOH molarity. Figure 1a shows a change in

slope of the log of water activity at ~5 M NaOH, and Figure 1b a change in slope of the log of NaOH activity coefficient also at ~5 M NaOH. This aligns roughly with the significantly different slopes below 1 M and above 10 M in Figure 1d. Eq. B-5 in Appendix B shows the explicit relationship between the log-log plots of Figure 1a-b and the semi-log plot of Figure 1d.

To establish an intuitive understanding of these phenomena, we make the following observations. The change in log of water activity and log of NaOH activity coefficient at ~5 M NaOH correlates with a drop by 2% of the molarity of water, and the molarity of water starts to decrease quickly as the molarity further increases. This indicates an insufficient supply of the water molecules present to hydrate the ions, preventing Na<sup>+</sup> and OH<sup>-</sup> ions from filling “empty space” in the solution as they do at lower concentrations indicated by the water molarity beginning to diminish. Thus, H<sub>2</sub>O molecules become unavailable for the desired electrochemical reactions, and the Na<sup>+</sup> and OH<sup>-</sup> ions develop an outsized availability for reaction, resulting from a high activity coefficient. In this case, the effect of OH<sup>-</sup> ions is to oppose the PtO reduction, i.e. to shift  $E_{\text{PtO red.}}$  to more cathodic potentials.

Relating this to CO<sub>2</sub>R, we see that the equilibrium potential for a reaction can be sensitive to solute and solvent activities, especially at high concentrations. Thus, for a GDE CL with uniform electric potential across the CL, gradients in electrolyte concentration across the CL would make gradients in reaction equilibrium potential. This would give a spatial distribution to the overpotential for each electrochemical reaction that is possible at the catalyst, which could have important implications for CO<sub>2</sub>R selectivity.

The dependence of the equilibrium potential for the electrochemical conversion of CO<sub>2</sub> to CO,  $E_{\text{CO}_2/\text{CO}}$ , on solvent and solute activities can be determined by the reaction

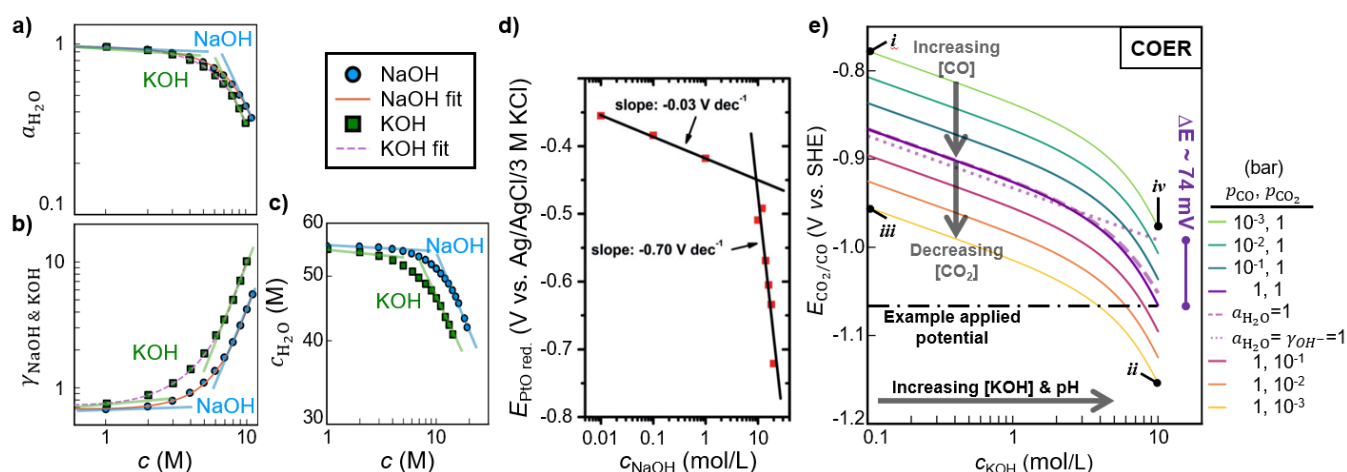
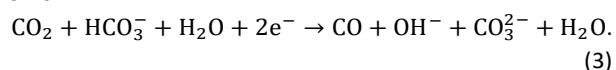
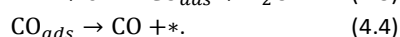
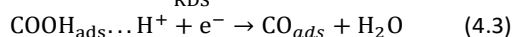
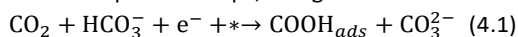


**Figure 1:** Dependence of a) solvent activity, b) solute activity, and c) solvent molarity on KOH molarity in aqueous solutions. d) Dependence of PtO/Pt equilibrium potential on NaOH molarity. e) Dependence of CO<sub>2</sub>/CO equilibrium potential on KOH molarity, CO<sub>2</sub> molarity, and CO molarity. Panel d) adapted with permission from<sup>19</sup>. Copyright 2018 Wiley VCH.

mechanism and rate-determining step (RDS). As a relevant example for CO<sub>2</sub>R, we consider nanostructured Ag catalysts, which are selective for the CO evolution reaction (COER) and offer reasonable comparisons to Cu and Au catalysts. To determine the rate-determining step (RDS) and thus the proper Nernst equation for  $E_{\text{CO}_2/\text{CO}}$  we reference recent work on COER on nanostructured Ag catalysts.<sup>26</sup> Despite this study's use of neutral pH solutions containing a buffer electrolyte (e.g. 0.5 M NaHCO<sub>3</sub>, pH 7.2) and low overpotentials, where the Tafel slope is not obscured by mass transport of reactants or products, it is thorough and the most relevant study to our system. In the proposed reaction mechanism, the first protonation was by the buffer anion HCO<sub>3</sub><sup>-</sup>, and second protonation by H<sub>2</sub>O; the second protonation was found to be the RDS. This gives the overall reaction of:



Broken down into sequential steps, this gives:

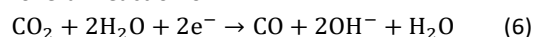


The reported equilibrium potential for this reaction mechanism and RDS is:<sup>26</sup>

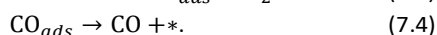
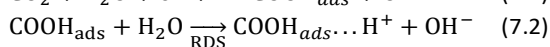
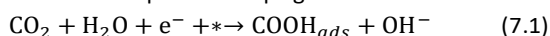
$$E_{\text{CO}_2/\text{CO}} = E_{\text{CO}_2/\text{CO}}^{0, \text{ nano-Ag}} + \frac{RT}{nF} \ln \frac{a_{\text{CO}_2} a_{\text{HCO}_3^-}}{a_{\text{CO}} a_{\text{CO}_3^{2-}} a_{\text{OH}^-}}. \quad (5)$$

Cu and Au have shown a similar dependence on buffer anions for CO<sub>2</sub> protonation.<sup>27-29</sup> Further work would be necessary to confirm that this mechanism and RDS apply to COER at GDEs, at high current densities, and in concentrated alkaline electrolytes.

For alkaline electrolytes above pH 10 or 11, where the equilibrium ratio of HCO<sub>3</sub><sup>-</sup> and CO<sub>3</sub><sup>2-</sup> favors the latter, only H<sub>2</sub>O would be available to protonate CO<sub>2</sub>. Assuming H<sub>2</sub>O for both protonation steps, but no change in the RDS for the Ag catalyst, would give an overall reaction of:



Broken down into sequential steps gives:



$E_{\text{CO}_2/\text{CO}}$  would then become:

$$E_{\text{CO}_2/\text{CO}} = E_{\text{CO}_2/\text{CO}}^{0, \text{ alkaline}} + \frac{RT}{nF} \ln \frac{a_{\text{CO}_2} a_{\text{H}_2\text{O}}}{a_{\text{CO}} a_{\text{OH}^-}^2}. \quad (8)$$

To validate this hypothesis, experiments that determine the Tafel slope and reaction order of CO<sub>2</sub>R electrodes in alkaline electrolyte would need to be performed, and compared with reaction mechanism calculations.<sup>26</sup> If the Tafel slope remained near 59 mV dec<sup>-1</sup>, the reaction rate became independent of HCO<sub>3</sub><sup>-</sup>, and the reaction order in OH<sup>-</sup> becomes 2, then Eq. 6 would likely be valid.

This example of COER at a Ag catalyst demonstrates that gradients in activity (i.e. concentration) of CO<sub>2</sub>, H<sub>2</sub>O, CO, HCO<sub>3</sub><sup>-</sup>,

CO<sub>3</sub><sup>2-</sup>, or OH<sup>-</sup> could shift the equilibrium potential of CO evolution significantly. If this gradient was extended spatially along the flow channel over a CL, and the CL had a uniform applied potential (i.e. perfect conductor), then the overpotential for the reaction would vary spatially along the CL, as detailed in the following section.

### Spatial variation along flow channels of reaction equilibrium potential

CO<sub>2</sub>R literature<sup>15,30</sup> has, so far, typically cited the simplified Nernst equation to describe how  $E_{\text{CO}_2/\text{CO}}$  changes with increasing KHCO<sub>3</sub> or KOH concentration. This equation depends only on pH and is usually written as:

$$E_{\text{CO}_2/\text{CO}} = -0.106 - 0.0591\text{pH}. \quad (9)$$

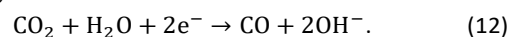
This approximation is accurate for electrolyte concentrations with water activity and solute activity coefficients of 1. Notably, this is only accurate for acidic or neutral electrolytes, for which the overall reaction can be written:



For alkaline electrolytes, (per derivation in appendix, Eq.'s A-7 through A-15) the simplified Nernst equation is given by:

$$E_{\text{CO}_2/\text{CO}} = -0.933 - 0.0591\text{pH}. \quad (11)$$

In this case, the overall reaction is written:



Here we clarify a common misnomer in CO<sub>2</sub>R literature. Since CO<sub>2</sub>R was originally done only in acidic or neutral electrolytes, but is now often done in alkaline electrolytes, it has become common for manuscripts to write Eq.'s 9 and 12 together, which is technically not accurate.

These simplified Nernst equations are special cases of Eq. 8. Figure 1e demonstrates the accuracy of the simplified Nernst equation for 0.1 to 10 M KOH. The dotted purple line shows the simplified Nernst equation (Eq. 11). The dashed purple line uses Eq. 8 and the experimental activity coefficient of KOH from Figure 1b, but with water activity still assumed to be 1. The solid purple line adds the effect of the water activity, using data from Figure 1a. The activity coefficients of CO<sub>2</sub> and CO are assumed to be 1, a valid assumption at standard temperature (298 K) for CO<sub>2</sub> below 2 mol% (i.e. below 1 M CO<sub>2</sub>)<sup>31</sup> and CO below 4.8 M CO (see CO activity coefficient derivation in Appendix A, Eq.'s A-1 to A-22, and Figure 3).<sup>32-37</sup> There are 20-50% variations in CO activity coefficient with changing temperature and electrolyte concentration and composition; consideration of these nuances lies outside the scope of this work, but could be worth future investigation. All purple lines have a ratio of  $p_{\text{CO}_2}/p_{\text{CO}} = 1$ .

From the purple lines in Figure 1e, the simplified Nernst equation is clearly quite accurate below 5 M KOH. At higher molarities, the simplified Nernst equation significantly underestimates the negative shift in  $E_{\text{CO}_2/\text{CO}}$  with increasing molarity, reaching a ~74 mV difference at 10 M between the simplified and activity dependent  $E_{\text{CO}_2/\text{CO}}$ .

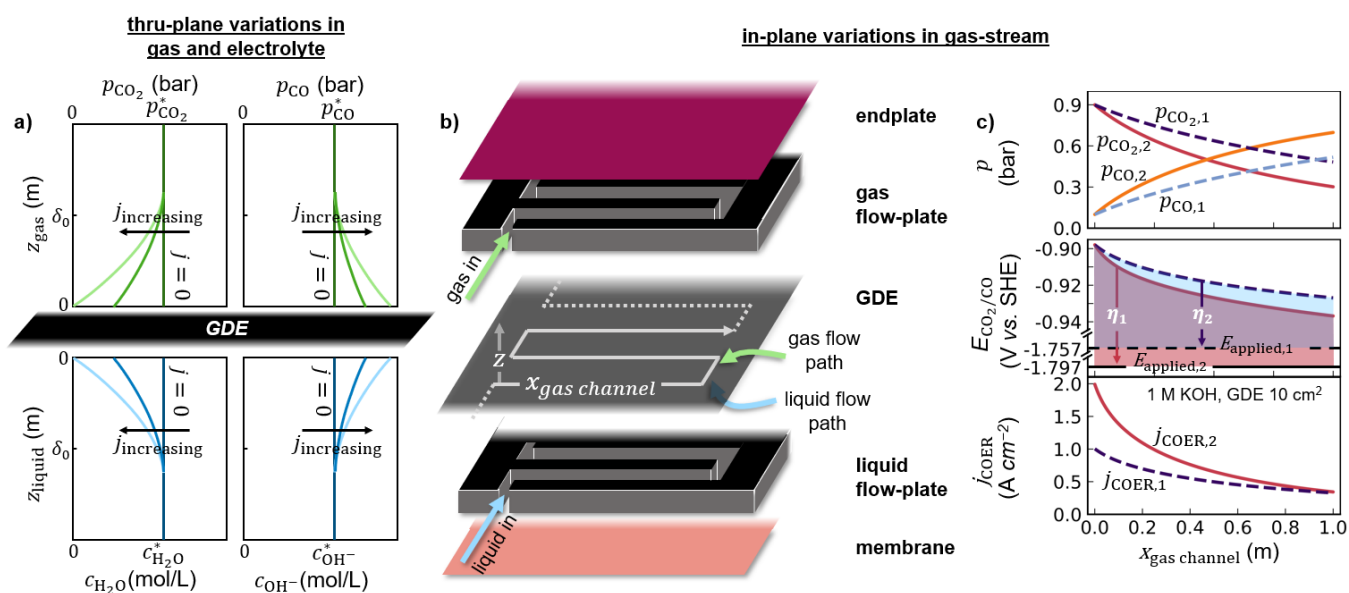
To demonstrate the influence of the ratio  $p_{\text{CO}_2}/p_{\text{CO}}$  on  $E_{\text{CO}_2/\text{CO}}$ ,  $\text{CO}_2$  and  $\text{CO}$  partial pressures were each varied to 1, 10, and 100 mbar while the other was held at 1 bar. These lines are plotted in Figure 1e, and demonstrate a -30 mV shift in  $E_{\text{CO}_2/\text{CO}}$  for each decade increase of  $p_{\text{CO}}$  or decade decrease in  $p_{\text{CO}_2}$ .

Figure 2a depicts the concentration gradient that develops vertically, through the plane of the GDE. With increasing current density, the reactant concentrations move towards zero and product concentrations move towards infinity at the CL surface. For an infinite bulk electrolyte or gas volume, the bulk partial pressures and concentrations will remain constant. Since  $E_{\text{CO}_2/\text{CO}}$  is defined for the case of zero current density, Eq. 8 uses these bulk concentrations.

Figure 2b shows a GDE for COER with a serpentine flow pattern for gas and liquid streams. Such flow fields have been suggested for large electrode devices.<sup>38–42</sup> In this case, the bulk electrolyte and gas are not infinite, and will vary in composition along the lateral flow path. At any given section of CL along this flow, the bulk concentrations for use in Eq. 8 are the result of up-stream conversion of reactants to products. This implies that if one short segment of GDE along the flow field could be turned down to zero current while the rest continued running, the reactant and product concentrations from upstream in the flow would define the “zero current” electrolyte and gas composition of this small segment.

We can use Figure 1e to surmise variations in  $E_{\text{CO}_2/\text{CO}}$  from hypothetical changes in electrolyte and gas stream composition in the flow field depicted in Figure 2b. For example, we consider a single-pass conversion of  $\text{CO}_2(\text{g})$  to  $\text{CO}(\text{g})$  in the gas stream high enough to cause a change from 1 bar  $\text{CO}_2 + 0.1$  bar  $\text{CO}$  to 0.1 bar  $\text{CO}_2 + 1$  bar  $\text{CO}$  in the dissolved gas of the CL. If a parallel flow of electrolyte had an increase in CL electrolyte molarity from 0.1 M KOH to 10 M KOH, then  $E_{\text{CO}_2/\text{CO}}$  would vary by 370 mV from inlet to outlet (the difference between annotations *i* and *ii* in Figure 1e). If, instead, the gas and liquid flows were anti-parallel, then, with the same variations in composition of the gas stream and electrolyte,  $E_{\text{CO}_2/\text{CO}}$  would vary by only 20 mV (difference between annotations *iii* and *iv* in Figure 1e). This suggests such anti-parallel flows could be quite advantageous for uniformity of current density in electrolyzers.

Figures 2b and 1e can also be interpreted from the perspective of overpotential,  $\eta = E_{\text{applied}} - E_{\text{CO}_2/\text{CO}}$ . For example, it is helpful to look at the case of the applied potential of -1.065 V vs. SHE, shown as a horizontal black dash-dot line in Figure 1e. Assuming  $\text{CO}_2$  and  $\text{CO}$  partial pressures in the gas flow are kept at partial pressures of 1 bar (Figure 1e purple lines), and the electrolyte at the inlet of a serpentine flow pattern was 0.1 M KOH, then  $\eta \approx -200$  mV would be expected. If the electrolyte concentration at the outlet reached 10 M KOH due to the  $\text{OH}^-$  production from  $\text{CO}_2\text{R}$ , but the common assumption was made that  $a_{\text{H}_2\text{O}} = 1$  and  $\gamma_{\text{OH}^-} = 1$ , then  $\eta \approx -80$  mV



**Figure 2:** General trends of activity, concentration, and partial pressure gradients near a GDE CL. a) (top) Schematic of gradient in partial pressure of  $\text{CO}_2$  and  $\text{CO}$  vertically from the CL into the gas stream at three current densities; (bottom) schematic of gradient in concentration of  $\text{H}_2\text{O}$  and  $\text{OH}^-$  vertically from the CL into the electrolyte stream at three current densities. b) Schematic of a GDE with serpentine flow fields above for gas and below for liquid,  $z$  represents thru-plane distance away from GDE surface (along surface normal),  $x$  represents in-plane distance along the flow path. c) Plots from a simple 1D model of  $\text{CO}_2$  and  $\text{CO}$  partial pressures,  $\text{CO}_2/\text{CO}$  equilibrium potential, and COER current density along parallel gas and liquid channels 1 m long.

would be expected. However, with accurate values of water and hydroxide activity used in Eq. 8, the 10 M KOH would actually have  $\eta \approx 0$  mV.

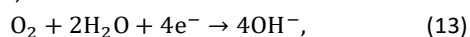
To add a change in partial pressure of CO<sub>2</sub> and CO to the hypothetical situation above, in the condition of 10 M KOH in the CL with  $\eta \approx 0$  mV, if  $p_{\text{CO}_2}$  was brought one decade below  $p_{\text{CO}}$  (a likely condition at the flow field outlet), this would cause  $\eta \approx +30$  mV (i.e. the reverse of the desired reaction).

Understanding the dependence of  $E_{\text{CO}_2/\text{CO}}$  on the local environment near a catalyst active site (referred to as the microenvironment) offers two advantageous opportunities. Electrolyzer design parameters, such as anti-parallel flows of gas and liquid, could help maintain uniform  $E_{\text{CO}_2/\text{CO}}$  throughout the CL. On the other hand, variations in the microenvironment could provide an opportunity to benefit cascade reactions, where the product from one part of the CL is the reactant for another part of the CL (e.g. CO generated from CO<sub>2</sub>R supporting ethylene production<sup>43</sup>).

Since increasing a product's partial pressure causes a negative shift in reaction potential, keeping a reactor saturated with a particular product could be a technique to prevent further production of that product, favoring a different one. For example, in a reactor designed to make CO for the purpose of producing syngas (a combination of CO and H<sub>2</sub>), the H<sub>2</sub> from a water electrolyzer (or recycle loop) could be fed into the electrolyte of the CO reactor to prevent production of H<sub>2</sub> in the CO reactor. This would prevent a reactor optimized for CO production from in-efficiently producing H<sub>2</sub>.

### Water activity effect on reaction rate

This section discusses the effect of water activity and solute activity coefficients on reaction rate. The effect of water and solute activity on reaction rate has been previously described for the well-studied ORR, a good model reaction for COER since both consume water to produce OH<sup>-</sup> and a gas product. The expected reaction is,



with current  $i$  given by,

$$i = -nFAr, \quad (14)$$

where  $n$  is the moles of electrons consumed per mol of O<sub>2</sub> or CO<sub>2</sub>,  $F$  the Faraday constant,  $A$  electrode area, and  $r$  reaction rate. The rate expression is,<sup>21</sup>

$$r_{\text{ORR}} = k^0 a_{\text{O}_2} a_{\text{H}_2\text{O}}^2 e^{-\alpha_c f \eta}, \quad (15)$$

where  $f=F/RT$ , and  $\alpha_c$  is the cathodic charge transfer coefficient.

In experiments that supplied O<sub>2</sub> to the electrode via dissolution into the electrolyte at a gas-liquid boundary 0.1-1  $\mu\text{m}$  from the electrode, the increasing NaOH concentration increased viscosity and decreased water activity; this slowed O<sub>2</sub> diffusion and decreased O<sub>2</sub> solubility, respectively, as demonstrated by oxygen depolarized electrodes (ODE) and scanning electrochemical microscopy (SECM) probes.<sup>21,22,44,45</sup>

The limited O<sub>2</sub> mass transport slowed the ORR current in high concentrations of aqueous NaOH, such as 10 M.

In these studies, the decrease in O<sub>2</sub> diffusion and solubility caused by increasing NaOH concentration obscured the effect of H<sub>2</sub>O activity on the ORR rate expression, shown in Eq. 15. Recent work circumvented this with a double-barrel nanopipette to supply O<sub>2</sub> locally to a Ag ORR catalyst.<sup>20</sup> The small separation between the O<sub>2</sub> source and Ag catalyst prevented solubility and viscosity from overshadowing the rate expression dependence on H<sub>2</sub>O activity. In this arrangement (per Table E-1) the current vs. voltage measurements made in 0.1, 5, and 10 M NaOH showed a reaction order of 2 in H<sub>2</sub>O ( $i_{\text{ORR}} \sim a_{\text{H}_2\text{O}}^2$ ).

To relate these results from this ORR study to CO<sub>2</sub>R, we consider, for example, the COER discussed above. Using the chemical reaction detailed in Eq.'s 3 and 4, where bicarbonate provides the first protonation of CO<sub>2</sub> and the assumed RDS was the second protonation, the current  $i_{\text{COER}}$  is given by Eq. 14 and the rate expression,

$$r_{\text{COER}} = k^0 \frac{a_{\text{CO}_2} a_{\text{H}_2\text{O}} a_{\text{HCO}_3^-}}{a_{\text{CO}_3^{2-}}} e^{-\alpha_c f \eta}. \quad (16)$$

Alternatively, for a more alkaline electrolyte, if the first protonation was from H<sub>2</sub>O as detailed in Eq.'s 6 and 7, but the RDS remained the second protonation, the current  $i_{\text{COER}}$  would be given by Eq. 14 and the rate expression,

$$r_{\text{COER}} = k^0 \frac{a_{\text{CO}_2} a_{\text{H}_2\text{O}}^2}{a_{\text{OH}^-}} e^{-\alpha_c f \eta}. \quad (17)$$

The first case would have reaction order -1 for CO<sub>3</sub><sup>2-</sup>, and 1 for CO<sub>2</sub>, H<sub>2</sub>O, and HCO<sub>3</sub><sup>-</sup>. The latter case would have reaction order -1 for OH<sup>-</sup>, 1 for CO<sub>2</sub>, and 2 for H<sub>2</sub>O. In either case, the reaction rate would be diminished at low water activity and high OH<sup>-</sup> activity. The HCO<sub>3</sub><sup>-</sup> protonation case would be indirect for the neutral buffer electrolyte: increasing OH<sup>-</sup> favors conversion of HCO<sub>3</sub><sup>-</sup> into CO<sub>3</sub><sup>2-</sup>, and thus an increasing CO<sub>3</sub><sup>2-</sup> concentration. This suggested lowering of hydroxide concentration also will mitigate CO<sub>2</sub> consumption by its conversion to bicarbonate and carbonate, important for energy efficiency of devices.<sup>18</sup>

Description	Definition	Symbol
<b>Model Parameters</b>		
Gas channel height	100 × 10 <sup>-6</sup> m	$y_{\text{gas}}$
Gas channel width	100 × 10 <sup>-6</sup> m	$z_{\text{gas}}$
Gas channel length	1 m	$x_{\text{gas}}$
Gas channel length segment	10 × 10 <sup>-6</sup> m	$x_{\text{seg}}$
Electrolyte	1 M KOH	$c$
Gas flow rate	1.67 × 10 <sup>-7</sup> m <sup>3</sup> s <sup>-1</sup> (10 ml min <sup>-1</sup> )	$v_{\text{gas\_flow}}$
Total gas pressure	1 bar	$P_{\text{total}}$

Rate constant <sup>6</sup>	$2.44 \times 10^{-8}$ moles <sub>CO</sub> s <sup>-1</sup> m <sup>-2</sup>	$k_{\text{CO}_2}^0$
Applied cathode potentials	-1.797 V vs SHE for 2 A cm <sup>-2</sup> -1.757 V vs SHE for 1 A cm <sup>-2</sup>	$E_{\text{applied}}$
Standard potential	-0.933 V vs SHE	$E_{\text{CO}_2/\text{CO}}^{0,\text{alkaline}}$
Symmetry factor	0.44	$\alpha_c$
Faraday constant	96,485 C mol <sup>-1</sup>	$F$
Gas constant	8.314 J mol <sup>-1</sup> K <sup>-1</sup>	$R$
Temperature	298 K	$T$
<u>Initial Conditions</u>		
Inlet partial pressure CO <sub>2</sub>	0.9 bar	$p_{\text{CO}_2,\text{in}}$
Inlet partial pressure CO	0.1 bar	$p_{\text{CO},\text{in}}$
<u>Model Equations</u>		
Gas segment volume	$x_{\text{seg}} \times y_{\text{gas}} \times z_{\text{gas}}$ [m <sup>3</sup> ]	$V_{\text{seg}}$
Time of gas segment over GDE segment	$V_{\text{seg}}/v_{\text{gas,flow}}$ [s]	$t_{\text{seg}}$
Partial Pressure CO <sub>2</sub>	$P_{\text{total}} - p_{\text{CO}}$ [bar]	$p_{\text{CO}_2}$
Thermodynamic constant	$F/RT$ [V <sup>-1</sup> ]	$f$
GDE segment area	$x_{\text{seg}} \times y_{\text{gas}}$ [m <sup>2</sup> ]	$A_{\text{CL,seg}}$
Equilibrium potential	Eq. 8 [V vs SHE]	$E_{\text{CO}_2/\text{CO}}$
Overpotential	$E_{\text{applied}} - E_{\text{CO}_2/\text{CO}}$ [V]	$\eta$
Current density	Eq. 14 [A m <sup>-2</sup> ]	$j$
Rate expression	Eq. 17 [moles <sub>CO</sub> s <sup>-1</sup> m <sup>-2</sup> ]	$r_{\text{COER}}$
Conversion of CO <sub>2</sub> to CO at a channel segment	$r_{\text{COER}} \times A_{\text{CL,seg}} \times t_{\text{seg}}$ [moles]	$\Delta_{\text{CO}_2 \rightarrow \text{CO}}$

**Table I:** 1D model parameters, initial conditions, and equations.

The above dependence of  $E_{\text{CO}_2/\text{CO}}$  and  $r_{\text{COER}}$  on the gas composition raises an important practical question: how does the current density vary along a flow field that is designed to achieve high single-pass conversion of CO<sub>2</sub> to CO? While clever cell design might mitigate gradients in H<sub>2</sub>O, OH<sup>-</sup>, and HCO<sub>3</sub><sup>-</sup> activities, it is an explicit objective of COER reactors to achieve high single pass conversion of CO<sub>2</sub> to CO and thereby avoid the financial and energy cost of their separation. To answer this question, we used the reaction mechanism and RDS of Eq. 17 in

a simple 1D model to calculate the change in gas composition,  $E_{\text{CO}_2/\text{CO}}$ , and  $j_{\text{COER}}$  along a serpentine flow field at a given applied potential and rate constant  $k^0$ .

The 1D model used a 1 m long channel with a 100 x 100 μm<sup>2</sup> cross-section (total GDE geometric surface area 10 cm<sup>2</sup>). For simplicity, the model assumed no thru-plane gradients in activities, concentrations, or partial pressures (*i.e.* the gas was assumed perfectly mixed in the vertical (*z*) direction); equilibration between anode and cathode was assumed ideal so that the electrolyte along the flow channel was a constant 1 M KOH; the GDE was assumed to be a perfect conductor so that the applied potential had no spatial variation along the channel. Equations, parameters, and initial conditions for this 1D model are summarized in Table I.

The results of the model reveal profiles of  $p_{\text{CO}_2}$ ,  $p_{\text{CO}}$ ,  $E_{\text{CO}_2/\text{CO}}$ , and  $j_{\text{COER}}$  along the flow field channel, depicted in Figure 2c. For a reactor operating at either 2 A cm<sup>-2</sup> or 1 A cm<sup>-2</sup> at the inlet, the model showed a drop to ~0.3 A cm<sup>-2</sup> at the outlet, a drop in  $\eta$  from -0.90 V to -0.86 V for 2 A cm<sup>-2</sup> (-0.86 V to -0.83 V for 1 A cm<sup>-2</sup>), and change in  $p_{\text{CO}_2}$  from 90% to 30% and  $p_{\text{CO}}$  from 10% to 70% for 2 A cm<sup>-2</sup> ( $p_{\text{CO}_2}$  from 90% to 48% and  $p_{\text{CO}}$  from 10% to 52% for 1 A cm<sup>-2</sup>). The effects of changing flow rate, gas channel width, and electrolyte concentration are depicted in Figures H-1 through H-3.

The model results demonstrated that, due to the thermodynamic equilibrium that defines  $E_{\text{CO}_2/\text{CO}}$  and the COER rate expression, a high conversion efficiency of CO<sub>2</sub> to CO necessitated a large variation in  $j_{\text{COER}}$  and  $\eta$  between the inlet and outlet of the reactor. Higher conversion efficiencies, which are desirable to avoid separation of CO<sub>2</sub> from CO, would have ever greater variations in  $j_{\text{COER}}$  and  $\eta$ .

The kinetic rate expression depended on the activities, concentrations, and partial pressures present at the CL during operation, not the bulk values as  $E_{\text{CO}_2/\text{CO}}$  did. Thru-plane gradients depicted in Figure 2a would likely be large for GDE's operating at 1 or 2 A cm<sup>-2</sup>, making our 1D model's assumption of no gradients a significant oversimplification. To model these thru-plane gradients would require 2D modeling of the gas and liquid flow channels, important future work to optimize high single-pass conversion CO<sub>2</sub>R electrolyzers. Measurement of these gradients would improve model accuracy and require probes with micrometer-scale thru-plane resolution, such as those for scanning electrochemical microscopy.<sup>19</sup>

### Operando study of ORR GDEs

Given the above effects of water and solute activity on electrochemical reactions, and the possibility for a reduction reaction in a GDE to produce OH<sup>-</sup> and alter the local electrolyte concentration, we now relate an operando study of an ORR GDE as a template for future CO<sub>2</sub>R studies.

The GDE architecture used in the ORR study<sup>21</sup> assumed a narrow (80 nm thick) interface separating dry and flooded agglomerates in the GDE, and calculated the concentration of

O<sub>2</sub> and various solutes as a function of distance into the flooded agglomerate region (from the gas-liquid interface). With no stirring of the bulk electrolyte, the dissolved O<sub>2</sub> concentration profile shrunk “almost to zero at the mass transport governed current density of  $j_{\text{ORR}} = -1.26 \text{ kA m}^{-2}$ ” ( $-126 \text{ mA cm}^{-2}$ ).<sup>21</sup> By stirring the electrolyte bulk, the accumulation of OH<sup>-</sup> and Na<sup>+</sup> in the flooded agglomerate was diminished. These operating conditions kept the dissolved O<sub>2</sub> concentration profile from shrinking to zero by maintaining high water activity and low viscosity, which provided high O<sub>2</sub> solubility and fast O<sub>2</sub> diffusion, respectively.

To study the dynamics and kinetics of the system, the applied potential was stepped to a more cathodic potential, and the simulated and experimental  $j_{\text{ORR}}$  vs. time response was compared. The results at these different potentials matched well and showed the time constant was “dominated by the mass transport of water and hydroxide ions between the reaction zone and the electrolyte bulk phase.”<sup>21</sup> Thus, the current response was determined by water and OH<sup>-</sup> mass transport, which was suggested to result from their effect on O<sub>2</sub> solubility and diffusion: upon increasing the applied potential, the current would spike, but then settle over ~80 s as OH<sup>-</sup> was generated, water activity decreased, viscosity increased, and O<sub>2</sub> supply decreased.

By observing the system’s dynamic response, this study of the ORR was able to experimentally confirm the local electrolyte concentration in the GDE that was predicted by modelling. Specifically, for the particular reactor studied,  $j_{\text{ORR}}$  was determined by the electrolyte concentration regulating O<sub>2</sub> transport to the catalyst. This insight into the local operando gas diffusion rate, electrolyte concentration, and reaction rate would also be able to help determine if water activity becomes a dominant factor in other types of reactors, such as those for CO<sub>2</sub>R. It thus serves as a strong model for future work on other electrocatalytic systems to better understand the local environment of CO<sub>2</sub>R in GDEs operating at high current densities.

### Experiment and modelling needs of CO<sub>2</sub>R

To our knowledge, the careful comparison of experimental and modelling results of electrode dynamics has not yet been reported for CO<sub>2</sub>R to the extent discussed above for ORR. Likewise, well-controlled studies such as that with the ORR at a nanopipette,<sup>20</sup> which singled out the effect of water activity on the ORR, could provide useful information about CO<sub>2</sub>R. This could aid future modelling efforts that attempt to account for variations in water and solute activity. These insights can guide understanding of the diverse multi-phase chemistry associated with CO<sub>2</sub>R: carbonate and bicarbonate equilibria,<sup>46,47</sup> CO<sub>2</sub> consumption by hydroxide, and multiple simultaneous product activities. These added complexities are absent in ORR, so explicit CO<sub>2</sub> centric studies would be needed.

Further work on the Tafel slope and the reaction order of various species in CO<sub>2</sub>R on GDEs would offer increased clarity

on how to improve reaction activity and energy efficiency. The latter is maximized if current is kept below the mass transport limited regime (i.e. in the kinetically limited regime), undesired side reactions are avoided, and kinetics are optimized by a low Tafel slope and high exchange current density. Compared to solid electrodes, GDEs have improved mass transport of CO<sub>2</sub> to allow ~1 A cm<sup>-2</sup> COER and have allowed use of concentrated KOH electrolytes that improved electrolyte ionic conductivity and suppressed HER.<sup>3,4,30</sup> To optimize performance, it should be ensured these improvements did not come at the cost of increased Tafel slope or lowered exchange current density. Tafel slopes are lowest when the RDS is near the end of the reaction steps. An RDS near the end of the reaction steps also causes the exchange current density (via the rate expression) to be positively correlated to reactant concentration and negatively correlated to product concentration, e.g. rate expressions in Eq.’s 15 and 16.

Little work has been done to measure Tafel slope or exchange current density of CO<sub>2</sub>R at GDEs for different electrolytes. One study of Cu GDEs showed increasing exchange current density and a slightly decreasing Tafel slope for increasing KHCO<sub>3</sub> and KOH concentration (up to 1 M KHCO<sub>3</sub> and 2 M KOH).<sup>48</sup> This trend is opposite that suggested in Eq.’s 15 or 16. When combined with the reported Tafel slope being 74-95 mV dec<sup>-1</sup>, this trend suggests the GDE RDS was an early step, either CO<sub>2</sub> binding or the first protonation. For comparison, solid nanostructured electrodes have demonstrated Tafel slopes of 60 mV dec<sup>-1</sup> on Ag<sup>26</sup> and 40 mV dec<sup>-1</sup> on Au,<sup>49-51</sup> which correlate with the RDS as the final step before release of the CO.

These solid nanostructured electrodes also showed high selectivity for COER over HER in comparison to planar electrodes. Limiting water supply to a planar solid electrode was recently demonstrated as another avenue to the high selectivity: a solid planar Au electrode in a water-in-salt electrolyte lowered water concentration and improved selectivity for COER over HER.<sup>52</sup> However, the Tafel slope was ~122-129 mV dec<sup>-1</sup>, correlating to the first electron transfer to CO<sub>2</sub>.

While GDEs have allowed increased CO<sub>2</sub> supply and lowered H<sub>2</sub>O concentration (via hydroxide electrolytes), the water-in-salt electrolyte lowered H<sub>2</sub>O concentration for a constant CO<sub>2</sub> supply. Both have achieved high selectivity for COER by increasing the concentration ratio of CO<sub>2</sub> to H<sub>2</sub>O, but also reported high Tafel slopes. Nanostructured catalysts with sufficient CO<sub>2</sub> and H<sub>2</sub>O, on the other hand, have shown high selectivity for COER with low Tafel slope. This suggests optimization of CO<sub>2</sub>R GDEs may come from improved catalysts and increased water supply (commensurate with the plentiful CO<sub>2</sub> available to the GDE). More information on Tafel slopes and reactant and product reaction orders of CO<sub>2</sub>R GDEs are needed to confirm or refute this projection.

It is relevant to compare the aforementioned analysis on water management and alkaline electrolytes to recent work that has used concentrated KOH (5-7 M) to report record CO<sub>2</sub>R



current densities as high as  $1 \text{ A cm}^{-2}$ .<sup>4</sup> From the perspective of this Perspective, the high current density with favorable selectivity for  $\text{CO}_2\text{R}$  over HER can be understood in the following manner. The ionic conductivity of KOH is maximized at 7 M, with lower concentrations limited by ion concentration and higher concentrations limited by viscosity.<sup>16</sup> Thus, the potential drop in the cell from ohmic losses, which can be large at a high current density like  $1 \text{ A cm}^{-2}$ , were minimized by using 5–7 M KOH. Regarding selectivity for  $\text{CO}_2\text{R}$  over HER, in comparison to H-cell reactors with neutral pH bulk electrolytes, the concentrated hydroxide maintains very low proton concentration while the GDE provides a large supply of  $\text{CO}_2$ ; together, these conditions favor  $\text{CO}_2\text{R}$  over HER, and the cell potential can be increased as needed to achieve high current densities without a  $\text{CO}_2$  mass transport limitation. However, the take-away message of this Perspective is that a low water supply and high hydroxide concentration will cause the first reaction step,  $\text{CO}_2$  binding to the catalyst, to be the RDS. If a sufficiently high supply of water and low concentration of hydroxide were provided, the RDS may be later in the reaction mechanism series of steps, which would provide a lower Tafel slope for the cathode and improved energy efficiency of the cell.

Computational modeling has demonstrated that the local pH can go above 14 and the  $\text{K}^+$  molarity go above 10 M at high  $\text{CO}_2\text{R}$  current densities, even for neutral pH bulk electrolytes, such as 0.5 M  $\text{KHCO}_3$ .<sup>1,6,15,28</sup> In addition, water films of  $\sim 3 \text{ nm}$  or less, which may be present in a GDE at the gas-liquid interface, have been predicted to have low water activity.<sup>53</sup> However, models of liquid electrolytes do not use activity-dependent reaction rates. These assumptions likely ignore important variations in reaction rate and equilibrium potentials throughout the CL, and thus cannot give a complete picture of the local reaction environment.

One example of a possible improvement from accounting for water and solute activity is the following: instead of needing artificial boundary conditions to capture the drop-off to zero of  $\text{CO}_2\text{R}$  current at the gas-liquid interface, as is typically done, inclusion of the water and solute activity effect on reaction rate may naturally produce this drop-off. Overall, including water and solute activity should provide more realistic insights into the current distribution and selectivity of GDEs for  $\text{CO}_2\text{R}$ .

## Conclusions

In conclusion, water supply in a GDE CL will control  $\text{CO}_2\text{R}$  in many important ways. The local electrolyte concentration, which is driven upwards by  $\text{CO}_2\text{R}$ , increases viscosity, slows diffusion, lowers conductivity of NaOH and KOH over 5–7 M, lowers  $\text{CO}_2$  solubility, increases the conversion rate of  $\text{CO}_2$  to (bi)carbonate, increases the solute activity coefficient, and lowers the water activity. The lowered water activity and increased solute activity should slow the COER rate and shift reaction equilibrium potentials. However, these effects have received little attention in experimental or modelling studies.

Since these effects may become increasingly important as  $\text{CO}_2\text{R}$  devices are pushed towards current densities above  $1 \text{ A cm}^{-2}$ , here we have detailed the likely role of water and solute activities in  $\text{CO}_2\text{R}$ , and surveyed work from relevant adjacent research fields to indicate what experimental and modelling work could provide a better understanding of  $\text{CO}_2\text{R}$ .

## Author Contributions

N. T. Nesbitt and W. A. Smith conceptualized the idea of the study and wrote the manuscript. N. T. Nesbitt ran the formal analysis and modelling.

## Conflicts of interest

There are no conflicts to declare.

## Acknowledgements

This work was authored in part by the National Renewable Energy Laboratory (NREL), operated by Alliance for Sustainable Energy, LLC, for the U.S. Department of Energy (DOE) under Contract No. DE-AC36-08GO28308. This work was supported by the Laboratory Directed Research and Development (LDRD) Program at NREL. The views expressed in the article do not necessarily represent the views of the DOE or the U.S. Government. The U.S. Government retains and the publisher, by accepting the article for publication, acknowledges that the U.S. Government retains a nonexclusive, paid-up, irrevocable, worldwide license to publish or reproduce the published form of this work, or allow others to do so, for U.S. Government purposes.

The authors thank Recep Kas for fruitful discussions on fundamentals of electrochemistry.

## Supplemental Information

See Supplemental Information for supporting derivations and figures.

## References

- 1 T. Burdyny and W. A. Smith, *Energy Environ. Sci.*, 2019, **12**, 1442–1453.
- 2 S. Ma, M. Sadakiyo, R. Luo, M. Heima, M. Yamauchi and P. J. A. Kenis, *Journal of Power Sources*, 2016, **301**, 219–228.
- 3 M. Jouny, W. Luc and F. Jiao, *Nat. Catal.*, 2018, **1**, 748–755.
- 4 F. P. García de Arquer, C.-T. Dinh, A. Ozden, J. Wicks, C. McCallum, A. R. Kirmani, D.-H. Nam, C. Gabardo, A. Seifitokaldani, X. Wang, Y. C. Li, F. Li, J. Edwards, L. J. Richter, S. J. Thorpe, D. Sinton and E. H. Sargent, *Science*, 2020, **367**, 661–666.
- 5 W. Ma, S. Xie, T. Liu, Q. Fan, J. Ye, F. Sun, Z. Jiang, Q. Zhang, J. Cheng and Y. Wang, *Nature Catalysis*, 2020, 1–10.
- 6 L.-C. Weng, A. T. Bell and A. Z. Weber, *Phys. Chem. Chem. Phys.*, 2018, **20**, 16973–16984.

- 7 L.-C. Weng, A. T. Bell and A. Z. Weber, *Energy Environ. Sci.*, 2019, **12**, 1950–1968.
- 8 C. Delacourt and J. Newman, *J. Electrochem. Soc.*, 2010, **157**, B1911.
- 9 G. Wen, B. Ren, J. T. Gostick and Z. Chen, *Meet. Abstr.*, 2020, **MA2020-01**, 1503.
- 10 K. Wu, E. Birgersson, B. Kim, P. J. A. Kenis and I. A. Karimi, *J. Electrochem. Soc.*, 2014, **162**, F23–F32.
- 11 Y. Chen, C. Xiang and N. Lewis, *J. Electrochem. Soc.*, , DOI:10.1149/1945-7111/ab987a.
- 12 L. C. Brée, M. Wessling and A. Mitsos, *Computers & Chemical Engineering*, 2020, **139**, 106890.
- 13 C. Georgopoulou, S. Jain, A. Agarwal, E. Rode, G. Dimopoulos, N. Sridhar and N. Kakalis, *Computers & Chemical Engineering*, 2016, **93**, 160–170.
- 14 A. Reyes, R. P. Janssonius, B. A. W. Mowbray, Y. Cao, D. G. Wheeler, J. Chau, D. J. Dvorak and C. P. Berlinguette, *ACS Energy Lett.*, 2020, **5**, 1612–1618.
- 15 F. Zhang and A. C. Co, *Angew. Chem. Int. Ed.*, 2020, **59**, 1674–1681.
- 16 A. L.-W. Woo, page 39. South Dakota State University, 1968.
- 17 M. Ma, E. L. Clark, K. T. Therkildsen, S. Dalsgaard, I. Chorkendorff and B. Seger, *Energy Environ. Sci.*, 2020, **13**, 977–985.
- 18 J. A. Rabinowitz and M. W. Kanan, *Nature Communications*, 2020, **11**, 5231.
- 19 A. Botz, J. Clausmeyer, D. Öhl, T. Tarnev, D. Franzen, T. Turek and W. Schuhmann, *Angew. Chem. Int. Ed.*, 2018, **57**, 12285–12289.
- 20 J. Clausmeyer, A. Botz, D. Öhl and W. Schuhmann, *Faraday Discuss.*, 2016, **193**, 241–250.
- 21 M. Röhe, A. Botz, D. Franzen, F. Kubanek, B. Ellendorff, D. Öhl, W. Schuhmann, T. Turek and U. Krewer, *ChemElectroChem*, 2019, **6**, 5671–5681.
- 22 G. Åkerlöf and G. Kegeles, 1940, **62**, 620–640.
- 23 J. Balej, *Int. J. Hydrogen Energy*, 1985, **10**, 233–243.
- 24 F. Pérez-Villaseñor, G. A. Iglesias-Silva and K. R. Hall, *Ind. Eng. Chem. Res.*, 2002, **41**, 1031–1037.
- 25 P. M. Sipos, G. Hefter and P. M. May, *J. Chem. Eng. Data*, 2000, **45**, 613–617.
- 26 J. Rosen, G. S. Hutchings, Q. Lu, S. Rivera, Y. Zhou, D. G. Vlachos and F. Jiao, *ACS Catal.*, 2015, **5**, 4293–4299.
- 27 H. Ooka, M. C. Figueiredo and M. T. M. Koper, *Langmuir*, 2017, **33**, 9307–9313.
- 28 K. Yang, R. Kas and W. A. Smith, *J. Am. Chem. Soc.*, 2019, **141**, 15891–15900.
- 29 A. Wuttig, Y. Yoon, J. Ryu and Y. Surendranath, *J. Am. Chem. Soc.*, 2017, **139**, 17109–17113.
- 30 C.-T. Dinh, T. Burdyny, M. G. Kibria, A. Seifitokaldani, C. M. Gabardo, F. P. García de Arquer, A. Kiani, J. P. Edwards, P. De Luna, O. S. Bushuyev, C. Zou, R. Quintero-Bermudez, Y. Pang, D. Sinton and E. H. Sargent, *Science*, 2018, **360**, 783–787.
- 31 L. W. Diamond and N. N. Akinfiev, *Fluid Phase Equilibria*, 2003, **208**, 265–290.
- 32 R. Sander, *Atmos. Chem. Phys.*, 2015, **15**, 4399–4981.
- 33 R. W. Meadows and D. J. Spedding, *Tellus*, 1974, **26**, 143–150.
- 34 S. B. Dake and R. V. Chaudhari, *J. Chem. Eng. Data*, 1985, **30**, 400–403.
- 35 E. Douglas, *J. Phys. Chem.*, 1967, **71**, 1931–1933.
- 36 M. M. T. Khan and S. B. Halligudi, *J. Chem. Eng. Data*, 1988, **33**, 276–278.
- 37 Chapter 9, [https://chem.libretexts.org/Bookshelves/Physical\\_and\\_Theoretical\\_Chemistry\\_Textbook\\_Maps/DeVoes\\_Thermodynamics\\_and\\_Chemistry/09%3A\\_Mixtures](https://chem.libretexts.org/Bookshelves/Physical_and_Theoretical_Chemistry_Textbook_Maps/DeVoes_Thermodynamics_and_Chemistry/09%3A_Mixtures), (accessed 6 November 2020).
- 38 D. M. Weekes, D. A. Salvatore, A. Reyes, A. Huang and C. P. Berlinguette, *Acc. Chem. Res.*, 2018, **51**, 910–918.
- 39 Y. C. Li, D. Zhou, Z. Yan, R. H. Gonçalves, D. A. Salvatore, C. P. Berlinguette and T. E. Mallouk, *ACS Energy Lett.*, 2016, **1**, 1149–1153.
- 40 D. Salvatore and C. P. Berlinguette, *ACS Energy Lett.*, 2020, **5**, 215–220.
- 41 D. A. Salvatore, D. M. Weekes, J. He, K. E. Dettelbach, Y. C. Li, T. E. Mallouk and C. P. Berlinguette, *ACS Energy Lett.*, 2018, **3**, 149–154.
- 42 X. Li and I. Sabir, *International Journal of Hydrogen Energy*, 2005, **30**, 359–371.
- 43 X. Wang, J. F. de Araújo, W. Ju, A. Bagger, H. Schmies, S. Kühl, J. Rossmeisl and P. Strasser, *Nature Nanotechnology*, 2019, **14**, 1063–1070.
- 44 H.-H. Yang and R. L. McCreery, *Journal of The Electrochemical Society*, 2000, 10.
- 45 C. Zhang, F.-R. F. Fan and A. J. Bard, *J. Am. Chem. Soc.*, 2009, **131**, 177–181.
- 46 X. Han, Z. Yu, J. Qu, T. Qi, W. Guo and G. Zhang, *J. Chem. Eng. Data*, 2011, **56**, 1213–1219.
- 47 L. B. Hitchcock, *Ind. Eng. Chem.*, 1934, **26**, 1158–1167.
- 48 H. Xiang, S. Rasul, K. Scott, J. Portoles, P. Cumpson and E. H. Yu, *Journal of CO2 Utilization*, 2019, **30**, 214–221.
- 49 N. T. Nesbitt, M. Ma, B. J. Trzeźniewski, S. Jaszewski, F. Tafti, M. J. Burns, W. A. Smith and M. J. Naughton, *J. Phys. Chem. C*, 2018, **122**, 10006–10016.
- 50 T. Saberi Safaei, A. Mephram, X. Zheng, Y. Pang, C.-T. Dinh, M. Liu, D. Sinton, S. O. Kelley and E. H. Sargent, *Nano Lett.*, 2016, **16**, 7224–7228.
- 51 S. Ringe, C. G. Morales-Guio, L. D. Chen, M. Fields, T. F. Jaramillo, C. Hahn and K. Chan, *Nature Communications*, 2020, **11**, 33.
- 52 Q. Dong, X. Zhang, D. He, C. Lang and D. Wang, *ACS Cent. Sci.*, 2019, **5**, 1461–1467.
- 53 J. O'M. Bockris and B. D. Cahan, *J. Chem. Phys.*, 1969, **50**, 1307–1324.